ORIGINAL PAPER

Electrochemiluminescent immunoassay for the determination of CA15-3 and CA72-4 using graphene oxide nanocomposite modified with CdSe quantum dots and Ru(bpy)$_3$ complex

Hosein Asbaghian-Namin[1,2] · Pari Karami[1] · Hamid Naghshara[2] · Danial Gholamin[3] · Mohammad Johari-Ahar[1,2]

Abstract

A novel immunoassay is introduced based on co-reactant enhancing strategy for the electrochemiluminescent (ECL) determination of CA15-3 and CA72-4 tumor markers in real samples. For the preparation of the signaling probe, CA15-3 and CA72-4 antibodies first were labeled using Ru(bpy)$_3^{2+}$-N-hydroxysuccinimide ester (Ru(bpy)$_3^{2+}$-NHS) and conjugated with L-cysteine capped cadmium selenide (CdSe) quantum dots. Finally, it was cross-linked with chitosan-grafted graphene oxide (GO@CS) nanocomposite. The capture probe was constructed by deposition of multi-walled carbon nanotubes (MWCNT) at the surface of dual-working gold screen–printed electrodes (MWCNT-dwSPE) and covalent attachment of capture CA15-3 and CA72-4 antibodies to MWCNT-dwSPE. ECL signals were recorded by applying cyclic potential ranging from 0.3 to 1.1 V (vs. pseudo-reference Ag/AgCl) at the scan rate of 100 mV.s^{-1}. This immunoassay was used for determination of CA15-3 and CA72-4 in real samples the detection limits of 9.2 μU.ml^{-1} and 89 μU.ml^{-1} within linear ranges of 10 μU.ml^{-1}–500 U.ml^{-1} and 100 μU.ml^{-1}–150 U.ml^{-1}, respectively. This immunoassay also showed acceptable accuracy with recoveries in the range 96.5–108 % and high reproducibility with RSD of 3.1 and 4.9.

Introduction

Electrochemiluminescent (ECL) immunoassays have been widely applied for the determination of disease biomarkers, especially tumor markers [1–3]. These assays have been of great interest for providing an adequate detection sensitivity, controllability of ECL reaction, and absence of external light source [4]. Despite offering these advantages, ECL-based immunoassays suffer from a limitation in miniaturization [5], mainly related

to the bulky size of the applied detectors (i.e., photomultipliers and charge-coupled devices) and their accessories [6] and lower efficiency of on-electrode ECL reactions [7].

The development of miniaturized platforms such as point-of-care (POC) testing, particularly for oncomarkers detection, provides ample opportunities for improving the quality of life and survival of cancer patients by rapid and out-of-lab/in-house diagnosis of tumor markers at early stages of cancer initiation or recurrences [5, 8].

A tumor marker is a molecule found in body fluids or tissues as an indicative of a cancer initiation, progression, or metastasis. Of these markers, CA15-3 [9] and CA72-4 [10] are used for early detection of cancer recurrences or failure of treatment modalities. CA15-3 and CA72-4, in combination, have also represented an accepted sensitivity, specificity, and accuracy for diagnosing malignant pleural effusion and discriminating ovarian cancer patients with a pelvic mass [11].

One of the main strategies to overcome the lower efficiency of on-electrode ECL reactions is the amplifying of in-electrode ECL signals [7]. In traditional sandwich-type ECL immunoassays, immunocomplexes are usually outside the outer

---

Hosein Asbaghian-Namin and Pari Karami contributed equally to this work.

✉ Mohammad Johari-Ahar
johary.pharmacy@gmail.com; m.johari@pharmacy.arums.ac.ir

1 Biosensor Sciences and Technologies Research Center, Ardabil University of Medical Sciences, Ardabil, Iran

2 School of Pharmacy, Ardabil University of Medical Sciences, Ardabil, Iran

3 Faculty of Physics, University of Tabriz, Tabriz, Iran

Helmholtz plane (OHP), and electron tunneling from a signaling probe to the electrode surface is imperfect [12]. Moreover, the dielectric effect of immunocomplex between the capture and signaling probe potentially reduces the whole participation of electrochemiluminophores in ECL reactions [13].

To increase the efficiency of in-electrode ECL reactions, the induction of the Faraday cage effect has the capability of extending OHP to integrate the signaling probe with the surface of the capture electrode [14]. As a result, electrons can freely flow in the cage and generate an efficient electrical conductivity. Additionally, the isopotential nature of the extended OHP results in the efficient excitation of labeled electrochemiluminophores [15].

To establish an efficient Faraday cage, the application of two-dimensional nanomaterials (2D) [16, 17], such as graphene oxide (GO) nanosheets, due to their unique electrical characteristics and functional groups for conjugation of secondary antibody, electrochemiluminophores, and ECL-enhancing nanomaterials is an ongoing research focus [18]. Of ECL-enhancing nanomaterials, semiconductor quantum dots (QDs) have shown fascinating characteristics. QDs are size-dependant luminescent nanoparticles ranging from 2 to 10 nm with tunable bandgap and easy-to-conjugate functional groups. However, the successful integration of capture and signaling probes of immunoassays to a single unit will provide a great potential for the development of next-generation sandwich-type ECL immunoassays [19].

In this work, we developed an ultrasensitive ECL immunoassay for the determination of CA15-3 and CA72-4 using GO nanocomposite modified with cadmium selenide QDs and ruthenium (Ru(bpy)$_3$) complex.

Materials and methods

Chemicals

N,N'-Dicyclohexylcarbodiimide (DCC); 1-ethyl-3-(3-dimethylaminopropyl) carbodiimide (EDC), N-hydroxysuccinimide (NHS), L-cysteine (L-cys), graphene oxide (GO), $K_4[Fe(CN)_6]$, $K_3[Fe(CN)_6]$, K_2HPO_4 and KH_2PO_4, and glutaraldehyde (GA) were purchased from Merck Co., (Darmstadt, Germany). Cadmium chloride, selenium (Se), sodium borohydride, sodium hydroxide, and sodium azide were obtained from Sigma-Aldrich Co. (Taufkirchen, Germany). MWCNT (purity > 80%, average diameter 9.5 nm, length ~1.5 μm, COOH content > 8.00 wt%) and Rutheniumbis (2,2′-bipyridine) (2,2′-bipyridine-4,4′-dicarboxylic acid) bis(hexafluorophosphate) ([Ru(bpy)$_2$(dcbpy)(PF$_6$)$_2$]) were obtained from Sigma-Aldrich (St. Louis, Missouri, USA). CA15-3 (orb81967) and CA72-4 (orb98842) oncomarker proteins, human CA15-3 ELISA kit (orb438314), human CA72-4 ELISA kit (orb438327), anti-CA15-3 antibody (orb308729) and CA72-4 antibody (orb98676) as signaling probe

antibodies (Abs), and anti CA15-3 antibody (orb633667) (Ab$_{15}$) and anti CA72-4 antibody (orb251667) (Ab$_{72}$) as capture probe antibodies were purchased from Biorbyt (Cambridge, England). In this study, distilled water (dH$_2$O) was used for preparation of buffers and reagents. Sodium silicate solution was prepared from Panreac Co. (Barcelona, Spain). Chitosan (Mw = 3 kDa, 90% degree of deacetylation) was prepared from Marline Bioengineering Co., Ltd., China.

Apparatus

ECL measurements were carried out by our homemade ECL system assembled by coupling a photomultiplier tube R1166 (Hamamatsu, Japan) with 910 PSTAT mini Metrohm Autolab. The integrated system was used to apply an operational voltage of 800 V to a photomultiplier tube (PMT), to amplify ECL signals from PMT, and to communicate with the homemade ECL software which was developed by visual basic 6 by our research group. The flow cell designed for holding SPE was used to carry out ECL experiments in the dark room with red light. A SONOPULS HD 3200 (Bandelin, Berlin, Germany) was used for sonication. UV-Vis and fluorescence spectra (photoluminescence (PL)) were recorded on a Shimadzu UV-1650PC spectrophotometer with a micro-cuvette and a Shimadzu spectrofluorophotometer (Shimadzu Corporation, Kyoto, Japan). The morphology of the synthesized nanomaterials was revealed by using a scanning electron microscope (SEM, MIRA3 FEG-SEM Tescan). Dual-working screen-printed electrodes (dwSPE) were prepared by printing the holographic pattern on copper-based PCB and electroplating a thin layer of gold (8 μm) on working electrodes (Zist Hesgar Fanavaran Aria (ZIFA) Co., Ardabil, IR). Reference electrodes were coated with Ag and then immersed in the sodium chloride (3 M).

CV and electrochemical impedance spectroscopy (EIS) measurements were performed using a frequency response analyzer (FRA) module-equipped PGSTAT302N (AutoLab, Metrohm Co., Schiedam, Netherlands). The Nova 1.8 software was used for method generation, data acquisition, and equivalent circuit fitting. To prepare dual-working screen-printed electrodes (dwSPE), working, counter, and reference electrodes were printed on a commercial single-sided PCB (printed circuit board); the counter electrode and working areas were coated with a thin layer of gold, while the reference electrode was coated with thin layer of silver. Then, the dwSPE was used for the preparation of Faraday cage-type ECL immunosensor.

Preparation of signaling probe (GO-CdSe-Ru-Abs)

Preparation of L-cys-capped CdSe quantum dots

L-cys-capped CdSe QDs were synthesized according to the previously reported procedure with minor modification [20].

Scheme 1 Illustration of the assembly of (**A**) the signaling probe and (**B**) capture probes. (**C**) Performance of the developed immunosensor. (**D**) ECL mechanism of luminophores
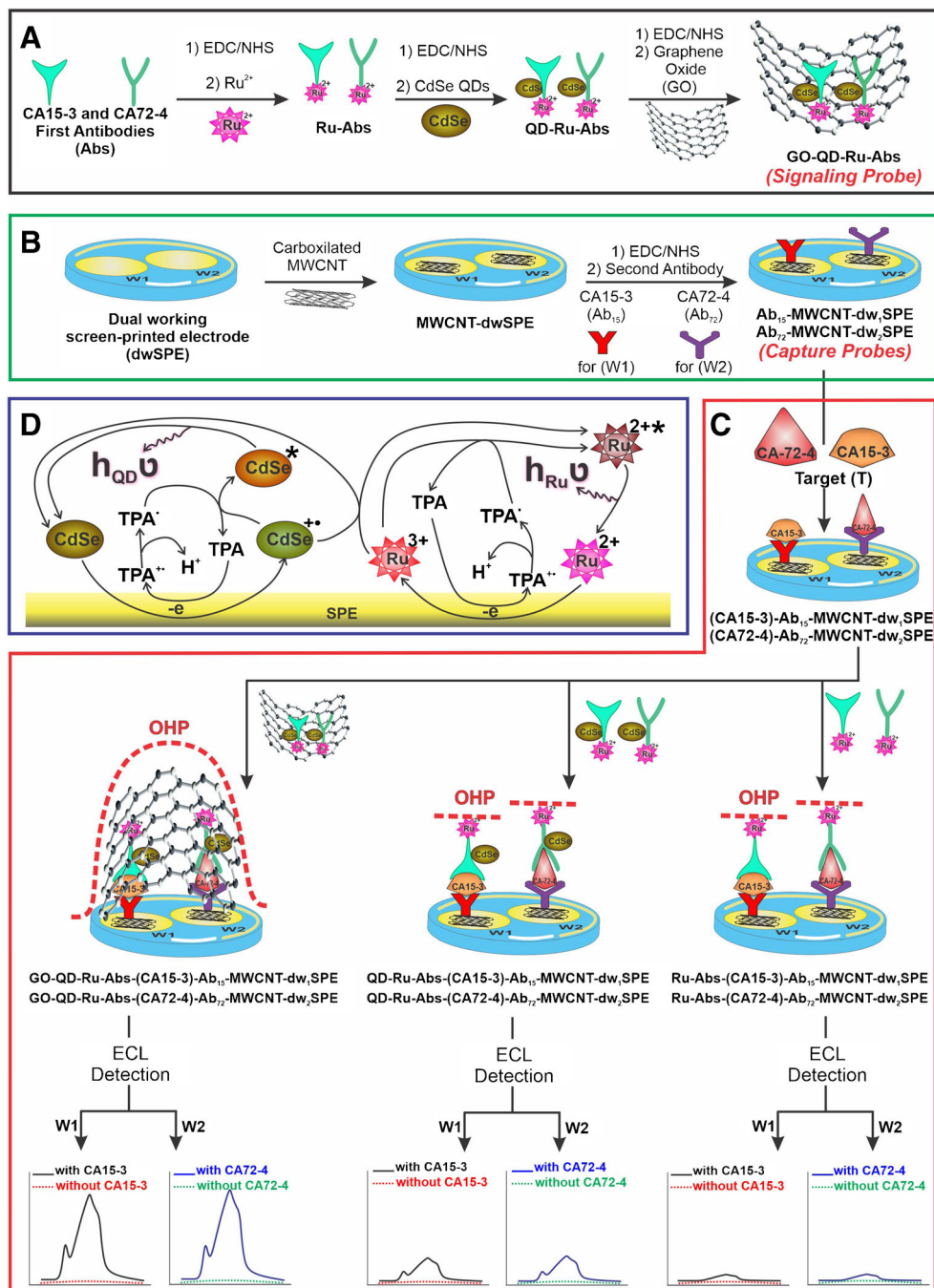
The detail of L-cys-capped CdSe QD synthesis is represented in the Supplementary information (S1).

Ru(bpy)$_3$$^{2+}$-NHS synthesis

To prepare Ru(bpy)$_3$$^{2+}$-NHS, Ru(bpy)$_2$(dcbpy)(PF$_6$)$_2$ was activated by NHS and N,N'-dicyclohexylcarbodiimide (DCC) in an anhydrous N,N'-dimethylformamide (DMF) [21]. The

detail of this synthesis is represented in the Supplementary information (S2).

The synthesis of Ru(bpy)$_3$$^{2+}$-labeled antibodies

After being removed from the refrigerator, CA15-3 and CA72-4 antibodies (Abs) were centrifuged at 5000g for 2 min (4 °C), purified from carrier proteins by size exclusion chromatography at 25 °C. The antibody solutions were diluted

to 1 mg.ml^{-1} by the addition of PBS (50 mM, pH = 7.9), and fresh Ru(bpy)$_3^{2+}$-NHS reagent (2 mM) was prepared by the addition of anhydrous DMF. For labeling antibody molecules, ruthenium:antibody molar ratio of 20:1 Ru(bpy)$_3^{2+}$-NHS was used (MW$_{IgG\ antibody}$ ≈ 150 kDa), and the DMF content did not exceed 10% of the total reaction volume. The tubes were covered by aluminum foil and shaken with a vortexer at 25 °C for 1 h. Then, 20 µl of glycine (2 M) was added to the solutions to stop the conjugation reactions, and after 15 min, unreacted Ru(bpy)$_3^{2+}$-NHS was removed by using a spin desalting column (40 kDa MWCO) equilibrated before with PBS. The concentrations of the collected Ru(bpy)$_3^{2+}$-labeled CA15-3 and CA72-4 antibody fractions (Ru-Abs) were determined using a BCA protein assay kit.

Preparation of hybrid structures of Ru-Abs-conjugated QDs (CdSe-Ru-Abs)

To synthesize hybrid structures of Ru-Abs-conjugated QDs (CdSe-Ru-Abs), 5 mg of lyophilized L-cys-capped CdSe QDs was dispersed gently in 100 µl of DMF and reacted with 23 mg of DCC and 12 mg of NHS in an ice/water bath. A total of 900 µl of Ru-Abs (1 mg.ml^{-1}) was transferred to the reaction mixtures, and the tubes were covered with an aluminum foil and shaken with a vortexer at 25 °C for 5 h. Twenty microliters of 2 M glycine was used to terminate the reactions after 30 min at room temperature. Finally, a spin desalting column (40 kDa MWCO) equilibrated before with the PBS was used to remove any unreacted materials.

Preparation of GO-conjugated CdSe-Ru-Abs (GO-CdSe-Ru-Abs)

First, chitosan-grafted GO (GO@CS) was prepared based on the methodology being reported in the literature [22]. The detail of this preparation is represented in the Supplementary information (S3). Scheme 1, panel A, represents the step-by-step preparation of the signaling probe (GO-CdSe-Ru-Abs).

Preparation of capture probes (Ab$_{15}$-MWCNT-dw$_1$SPE and Ab$_{72}$-MWCNT-dw$_2$SPE)

Five milligrams of MWCNT was added to 5 ml of dH$_2$O and dispersed homogenously by sonication (25 W) for 10 min. Next, 9 µl of the MWCNT suspension (1 mg.ml^{-1}) was uniformly layered by drop-casting on each working area of dwSPE and dried at 60 °C (MWCNT-dwSPE). The MWCNT-dwSPE was rinsed with dH$_2$O for removing unattached MWCNT.

For activation/conjugation of carboxylic acid groups, MWCNT-dw$_1$SPE and MWCNT-dw$_2$SPE were immersed in 5 ml of a borate buffer (pH = 9) containing NHS (10 mg.ml^{-1}) and EDC (20 mg.ml^{-1}) under stirring (60 rpm) at dark for 30 min. Secondary antibodies (Ab$_{15}$ and Ab$_{72}$) were covalently attached to the activated MWCNT-dw$_1$SPE and MWCNT-dw$_2$SPE by immersing in 1.5 ml of Ab$_{15}$ and Ab$_{72}$ solutions (50 µg.ml^{-1}) in 2-ml microtubes and shaking at 8 °C and dark for overnight (Ab$_{15}$-MWCNT-dw$_1$SPE and the Ab$_{72}$-MWCNT-dw$_2$SPE). The storage of capture probes was in 2-ml microtubes containing 0.1% (w/v) of sodium azide in a 0.1 M PBS (pH = 7.4) at 8 °C. Scheme 1, panel B, represents the step-by-step assembling of the capture probes.

Analysis of CA15-3 and CA72-4 using the developed immunosensor

To reveal the performance of the developed immunosensor, 50 µl of different standard concentrations of CA15-3 and CA72-4 (0.0001, 0.001, 0.01, 0.1, 1, 10, 100, 500 U.ml^{-1}), prepared in PBS (0.1 M, pH = 7.4), was placed on the capture probes (Ab$_{15}$-MWCNT-dw$_1$SPE and Ab$_{72}$-MWCNT-dw$_2$SPE). Next, the electrodes were gently shaken at 25 °C for 60 min and rinsed with PBS (0.1M, pH = 7.4) three times. The working areas of the electrodes were incubated with 50 µl of the signaling probe (GO-CdSe-Ru-Abs) under mild shaking at 25 °C for 60 min. After washing with PBS (0.1 M, pH = 7.4) to remove unbound probes, 100 µl of TPA (0.25 mM) in PBS (0.1M, pH = 7.4) was placed on of the electrodes, and ECL signals were recorded. Scheme 1, panel C, illustrates the performance of the developed immunosensor. To plot the calibration curve, ECL signals from different standard concentrations of CA15-3 and CA72-4 were recorded by applying CV scanning in the range of 0.3–1.1 V (vs. pseudo-reference Ag/AgCl) at the scan rate of 100 mV.s^{-1}. The measurements were triplicate (3 cyclic scannings for each measurement).

Real sample analyses

To assess the applicability of the immunosensor in direct detection of CA15-3 and CA72-4 in blood serum samples, CA15-3 and CA72-4 antigens were spiked to the serum samples with different concentrations. The detail of this analysis is represented in the Supplementary information (S5).

EIS analyses

EIS measurements were performed at the formal potential of 0.17 V (Fe(CN)$_6^{4-/3-}$) and frequency range of 0.1 Hz to 100 kHz. EIS results were obtained in a PBS (0.1 M, pH 7.4) containing K$_3$[Fe(CN)$_6$]/K$_4$[Fe(CN)$_6$] (5 mM, 1:1) and represented in the form of Nyquist plot after fitting to appropriate equivalent circuit.

Results and discussion

Characterization

UV-vis absorption and photoluminescence behavior of luminophores

The maximum intensity of UV-vis absorption and photoluminescence (PL) for unconjugated $Ru(bpy)_3^{2+}$-NHS (Ru^{2+}) was observed at 354 nm and 576 nm (Fig. S1, panels A, and B, curves a, Supplementary information), respectively. Also, the maximum absorption and PL intensity of diluted QDs (20-fold) was recorded at 365 and 525 nm (Fig. S1, panel A and panel B, curves b). The results show that energy transfer between Ru^{2+} and QDs is impossible because there is no overlap between the absorption and emission spectra.

Cyclic voltammetry and ECL behavior of luminophores

The electrochemical behavior of the bare and modified electrodes was investigated by CV and ECL by applying cyclic scanning in 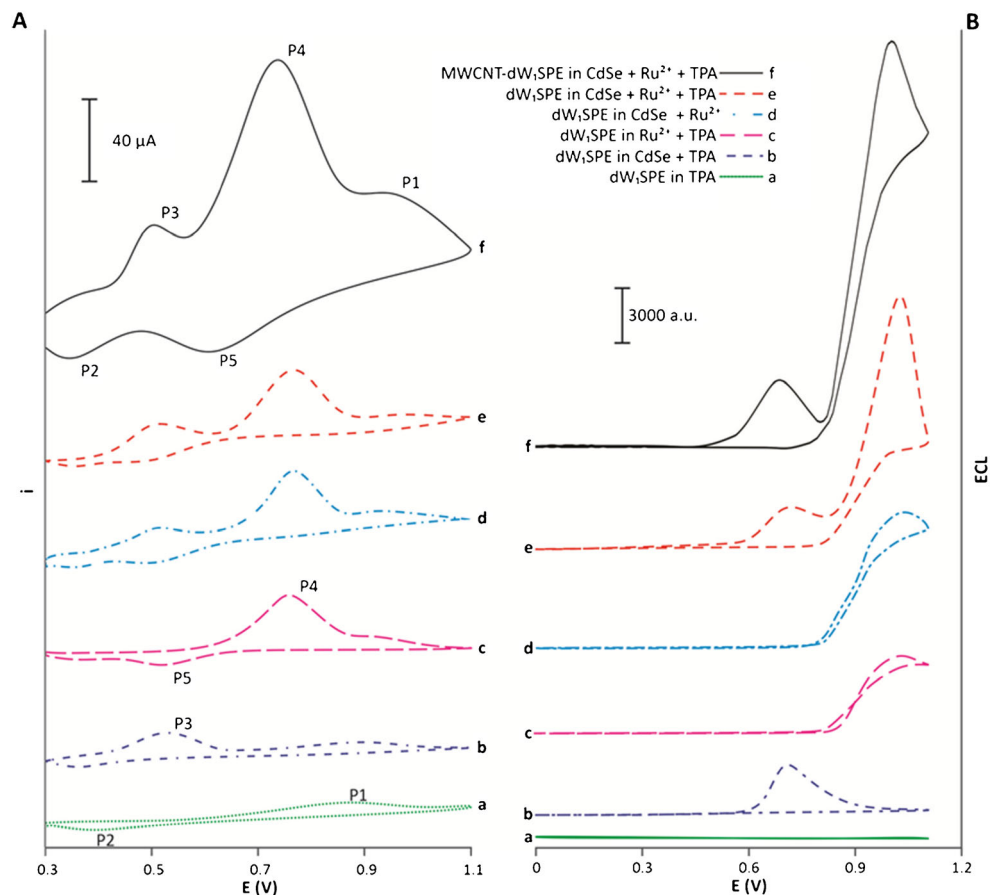the potential range of 0.3–1.1 and 0–1.1 V (vs. pseudo-reference Ag/AgCl) at the scan rate of 100 mV.s^{-1}, respectively (Fig. 1, panels A and B).

As presented in Fig. 1 (panel A, curve a), the CV of the bare Au-dwSPE of PBS (0.1 M, pH = 7.4) containing TPA (0.25 mM) in the absence of any luminophore represented only one broad anodic peak at about 0.87 V (vs. Ag-PR-SPE) (P1) and one cathodic peak (P2) at about 0.38 V, corresponding to the oxidation of gold metal (Au) to gold(III) (Au^{3+}) and the reduction Au^{3+} to Au, respectively. In the absence of luminophores, no ECL signals were recorded in the PBS (0.1 M, pH = 7.4) containing 0.25 mM TPA (Fig. 1, panel B, curve a).

In the presence of CdSe QDs, one anodic peak (P3) appeared at about 0.52 V (Fig. 1, panel A, curve b), and an ECL signal was recorded at 0.68 V (Fig. 1, panel B, curve b). Moreover, when existing Ru^{2+}, anodic (P4) and cathodic peaks (P5) were recorded at 0.75 V, and 0.52 V, respectively (Fig. 1, panel A, curve c), and an ECL signal appeared at 1.02 V (Fig. 1, panel B, curve c).

When scanned towards positive potentials, two anodic peaks at 0.52 and 0.75 V were observed (Fig. 1, panel A, curve d), and ECL signals were acquired from CdSe and Ru^{2+} at 1.02 V (Fig. 1, panel B, curve d), which was

Fig. 1 (**A**) Cyclic voltammograms and (**B**) cyclic ECL curves of dwSPE in 0.1 M PBS (pH 7.4) containing TPA (a); CdSe and TPA (b); Ru^{2+} and TPA (c); CdSe and Ru^{2+} (d); CdSe, Ru^{2+}, and TPA (e); and MWCNT-dwSPE in 0.1 M PBS (pH 7.4) containing CdSe, Ru^{2+}, and TPA (f)
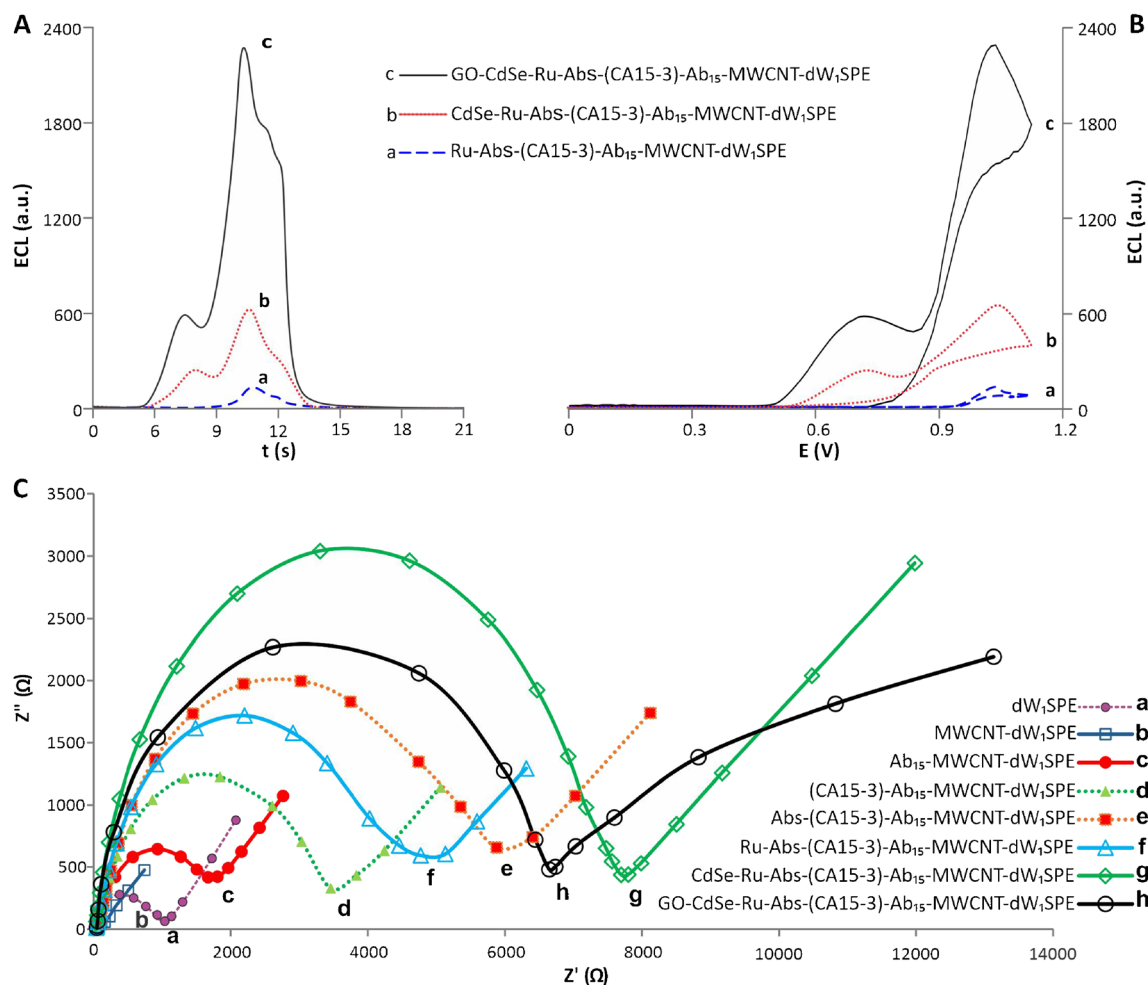
Fig. 2 (**A**) ECL time curve and (**B**) cyclic ECL curve of Ru-Abs-(CA15-3)-Ab$_{15}$-MWCNT-dw$_1$SPE (a), CdSe-Ru-Abs-(CA15-3)-Ab$_{15}$-MWCNT-dw$_1$SPE (b), GO-CdSe-Ru-Abs-(CA15-3)-Ab$_{15}$-MWCNT-dw$_1$SPE (c). (**C**) EIS analysis for step-by-step fabrication of immunosensor; dw$_1$SPE (**a**), MWCNT-dw$_1$SPE (**b**), Ab$_{15}$-MWCNT-dw$_1$SPE (**c**), (CA15-3)-Ab$_{15}$-MWCNT-dw$_1$SPE (**d**), Abs-(CA15-3)-Ab$_{15}$-MWCNT-dw$_1$SPE (**e**), Ru-Abs-(CA15-3)-Ab$_{15}$-MWCNT-dw$_1$SPE (**f**), CdSe-Ru-Abs-(CA15-3)-Ab$_{15}$-MWCNT-dw$_1$SPE (**g**), GO-CdSe-Ru-Abs-(CA15-3)-Ab$_{15}$-MWCNT-dw$_1$SPE (**h**)

significantly stronger than that of TPA and Ru^{2+} in PBS (0.1 M, pH = 7.4). In the absence of TPA, CdSe QDs act as a co-reactant for Ru^{2+} even stronger than TPA.

In the presence of TPA, two ECL signals at 0.68 V and 1.02 V can be observed (Fig. 1, panel B, curve e). It seems that TPA acts as a co-reactant for both CdSe and Ru^{2+}, while CdSe acts as a co-reactant for Ru^{2+}. We observed that using a bare dwSPE could produce weak ECL signals for CdSe and Ru$_2{}^+$, but after modification with MWCNT, dwSPE showed better conductivity and amplified CV and ECL signals (Fig. 1, panels A and B, curves f). In Fig. S2 (Supplementary information), PL properties of Ru^{2+} and CdSe in the form of the mixture have been represented, revealing that no chemical reaction occurred between CdSe and Ru^{2+}. This proves that the only reason for observing the light emission from co-reactant effect of CdSe is an electrochemical reaction between Ru^{2+} and CdSe QDs.

ECL mechanism of luminophores

The result of ECL measurements shows that Ru^{2+} is the key luminophore in the anodic ECL, and CdSe QDs alone can only produce a weak ECL signal even in the presence of TPA. This means that the electrochemical oxidation of Ru^{2+} to Ru^{3+} is catalyzed by QDs, resulting in the formation of QDs$^{+\bullet}$ as a powerful reducing agent. Then, transferring an electron between Ru^{3+} and QDs$^{+\bullet}$ leads to the generation of Ru^{2+*} (excited state) and emission of photons with the wavelength of ~576 nm. Additionally, TPA is electro-chemically oxidized to form the reducing agent (TPA$^{\bullet}$). TPA$^{\bullet}$ has the capability of reacting with Ru^{3+} and QDs$^{+\bullet}$ to produce Ru^{2+*} and QDs* (excited states), which in turn emit light at ~576 nm and ~525 nm, respectively. The inhibition mechanism (Scheme 1, panel D) is outlined below:
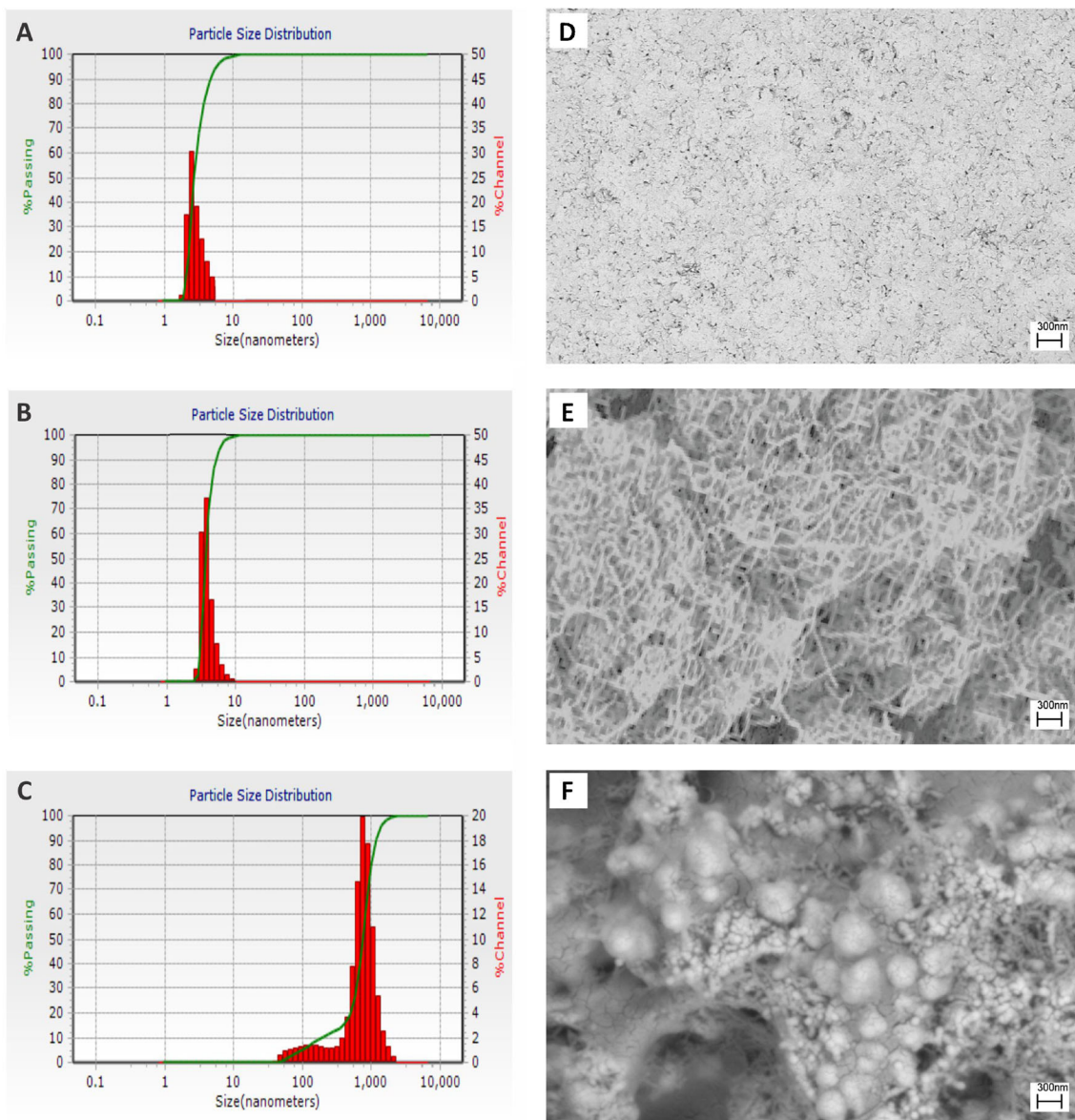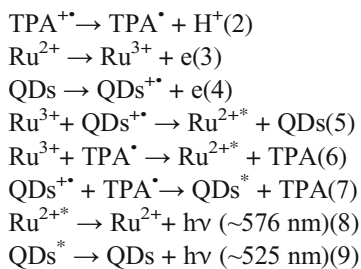
$$TPA \rightarrow TPA^{+\bullet} + e \quad (1)$$

Fig. 3 DLS analysis for (**A**) CdSe, (**B**) CdSe-Ru-Abs, and (**C**) GO-CdSe-Ru-Abs. SEM analysis for (**D**) dw$_1$SPE, (**E**) Ab$_{15}$-MWCNT-dw$_1$SPE, and (**F**) GO-CdSe-Ru-Abs-(CA15-3)-Ab$_{15}$-MWCNT-dw$_1$SPE

$$TPA^{+\bullet} \to TPA^{\bullet} + H^{+} \quad (2)$$
$$Ru^{2+} \to Ru^{3+} + e \quad (3)$$
$$QDs \to QDs^{+\bullet} + e \quad (4)$$
$$Ru^{3+} + QDs^{+\bullet} \to Ru^{2+*} + QDs \quad (5)$$
$$Ru^{3+} + TPA^{\bullet} \to Ru^{2+*} + TPA \quad (6)$$
$$QDs^{+\bullet} + TPA^{\bullet} \to QDs^{*} + TPA \quad (7)$$
$$Ru^{2+*} \to Ru^{2+} + h\nu \ (\sim 576 \ nm) \quad (8)$$
$$QDs^{*} \to QDs + h\nu \ (\sim 525 \ nm) \quad (9)$$

ECL behavior of immunosensor

ECL responses of the immunosensor after each step of modification were studied. Extremely weak ECL was observed at the Ru-Abs-(CA15-3)-Ab$_{15}$-MWCNT-dw$_1$SPE (Fig. 2,

panels A and B, curves a) and Ru-Abs-(CA72-4)-Ab$_{72}$-MWCNT-dw$_2$SPE (Fig. S3, panels A and B, curves d, Supplementary information), which is due to the anodic ECL of Ru^{2+} with TPA. When the CdSe QDs were added to the signaling probe, an amplified ECL signal was obtained, which was due to the co-reactant effect of CdSe QDs on Ru^{2+}-TPA ECL system (Fig. 2, panels A and B, curves b, Fig. S3, panels A and B, curves e). When GO was used as a grid for the signaling probe, ECL signals were intensified even greater than that of the previous step. One of the possible reasons for such amplification is the Faraday cage effect of GO (Fig. 2, panels A and B, curves c, Fig. S3, panels A and B, curves f). Another possible explanation for this observation is that GO sheets provide larger specific surface area for loading more
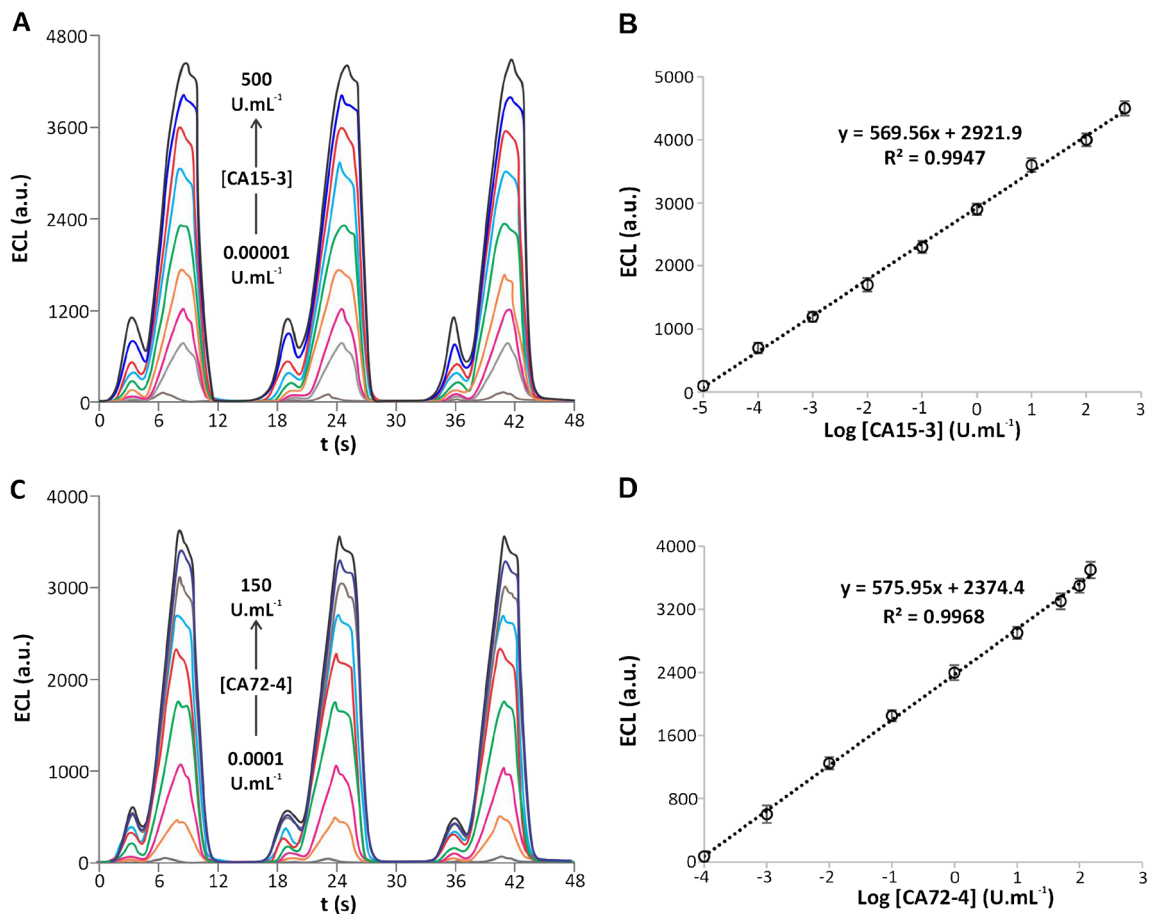
Fig. 4 The ECL time curve of the immunosensor incubated with different concentrations of (**A**) CA15-3 (0.00001, 0.0001, 0.001, 0.01, 0.1, 1, 10, 100, 500 U.ml^{-1}) and (**C**) CA72-4 (0.0001, 0.001, 0.01, 0.1, 1, 10, 50, 100, 150 U.ml^{-1}). Corresponding logarithmic calibration curve for ECL signal of the immunosensor after the incubation in different concentrations of (**B**) CA15-3 and (**D**) CA72-4

luminescent labels to both sides of sheets, thus resulting in a significant ECL enhancement. It makes possible more Ru^{2+} and CdSe QDs to be confined in the cage and became

effective, thus enhancing sensitivity. Other studies have shown the key role of GO nanosheet in extending OHP of the electrode surface [16–18, 23].

Table 1 Comparison of the proposed method with previously published methods used for detection of CA15-3 and CA72-4.

Analyte	Sensor configuration	LOD (U.ml^{-1})	LDR (U.ml^{-1})	Technic	Ref.
CA15-3	PAMAM-ZNs-Ab$_2$-(Ag)-Ab$_1$-AuNPs-GCE	0.0333	0.1–120	ECL	[28]
	CQDs-AuNPs-GO-Ab$_2$-(Ag)-Ab$_1$-AgNPs-GCE	0.0017	0.005–500	ECL	[29]
	PAMAM-CdTe@CdS-Ab$_2$-(Ag)-Ab$_1$-GA-Fe$_3$O$_4$@SiO$_2$-ITOE	1×10^{-5}	1×10^{-4}–100	ECL	[30]
	Pt-Lum-Ab$_2$-(Ag)-Ab$_1$-MOC-GCE	2×10^{-4}	5×10^{-4}–500	ECL	[31]
	GO-CdSe-Ru-Ab$_2$-(Ag)-Ab$_1$-MWCNT-dw$_1$SPE	9.2×10^{-6}	1×10^{-5}–500	ECL	This work
CA72-4	PANi-AuAMNPs-Ab$_2$(Ag)Ab$_1$-NPG-GCE	0.1	2–200	A	[32]
	PtPd-Fe$_3$O$_4$-Ab$_2$-(Ag)-Ab$_1$-rGO-TEPA-GCE	3×10^{-4}	0.001–10	CV	[33]
	Ab-PPy-GO-Ag$_2$Se@CdSe-GCE	2.1×10^{-5}	1×10^{-4}–20	ECL	[31]
	GO-CdSe-Ru-Ab$_2$-(Ag)-Ab$_1$-MWCNT-dw$_2$SPE	8.9×10^{-5}	1×10^{-4}–150	ECL	This work

A amperometry, *Ab* antibody, *Ag* antigen (analyte), *AgNPs* silver nanoparticles, *AuAMNPs* gold asymmetric multicomponent nanoparticles, *AuNPs* gold nanoparticles, *CQDs* carbon quantum dots, *ECL* electrochemiluminescence, *GA* glutaraldehyde, *GCE* glassy carbon electrode, *GO* graphene oxide, *ITOE* ITO electrode, *Lum* luminol, *MOC* mesoporous carbon nanospheres, *NPG* nanoporous gold, *PAMAM* polyamidoamine, *ZNs* ZnO nanorods, *PANi* poly(aniline), *PPy* polypyrrole, *rGO* reduced graphene oxide, *SPE* screen-printed electrode, *TEPA* tetraethylene pentamine

Fig. 5 A Interference study for immunosensor. The recorded ECL signals by the developed immunosensor for 0.1 U.ml^{-1} CA15-3 and CA72-4, 1000 ng.ml^{-1} Myo, 40 ng.ml^{-1} PSA, 1 ng.ml^{-1} VEGF, 100 ng.ml^{-1} EGFR, 200 ng.ml^{-1} COR, 20 ng.ml^{-1} NSE, 100 mg.ml^{-1} HSA, and 20 ng.ml^{-1} CEA. **B** ECL time curve of immunosensor for (a) 0.1 U.ml^{-1} CA15-3 and (b) CA72-4 during 15 consecutive cyclic potential
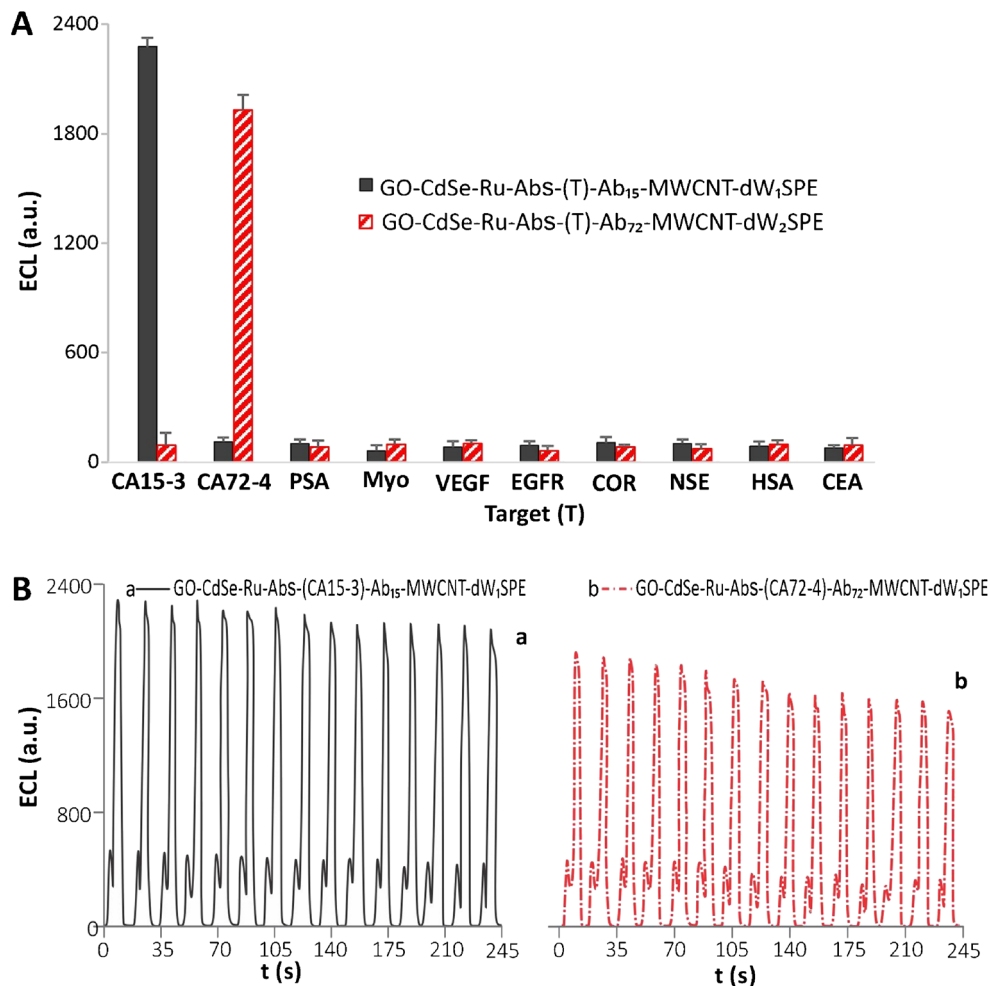
EIS analysis

The fabrication of immunosensor in each step was monitored by EIS. The diameter of semicircles in the Nyquist plot as an indicative of charge transfer resistances (R_{ct}) or real ohmic resistance of electrodes reveals the conductivity and layer-by-layer settlement of probes.

Figure 2, panel C, and Fig. S4 (Supplementary information) shown in the form of Nyquist plot, represents a step-by-step analysis of immunosensor fabrication. Steps included dw$_1$SPE (a), MWCNT-dw$_1$SPE (b), Ab$_{15}$-MWCNT-dw$_1$SPE (c), (CA15-3)-Ab$_{15}$-MWCNT-dw$_1$SPE (d), Abs-(CA15-3)-Ab$_{15}$-MWCNT-dw$_1$SPE (e), Ru-Abs-(CA15-3)-Ab$_{15}$-MWCNT-dw$_1$SPE (f), CdSe-Ru-Abs-(CA15-3)-Ab$_{15}$-MWCNT-dw$_1$SPE (g), GO-CdSe-Ru-Abs-(CA15-3)-Ab$_{15}$-MWCNT-dw$_1$SPE (h), Ab$_{72}$-MWCNT-dw$_2$SPE (i), (CA72-4)-Ab$_{72}$-MWCNT-dw$_2$SPE (j), and GO-CdSe-Ru-Abs-(CA72-4)-Ab$_{72}$-MWCNT-dw$_2$SPE (k). The R_{ct} of the bare dw$_1$SPE (curve a) was significantly reduced after MWCNT deposition (curve b). This means that MWCNT-dw$_1$SPE, in contrast to the bare dw$_1$SPE represents much more conductivity, which can amplify electrochemical signals. Once MWCNT-dw$_1$SPE was decorated with capture CA15-3 antibody (Ab$_{15}$), R_{ct} was significantly increased, which is due to the dielectric effect layered antibody molecules (curve c). After CA15-3 antigen molecules and then bare secondary CA15-3 antibody molecules (curve e) were attached to the Ab$_{15}$-MWCNT-dw$_1$SPE, R_{ct} values were increased (curve d) because of the double-layer resistance of protein molecules. The incubation of (CA15-3)-Ab$_{15}$-MWCNT-dw$_1$SPE with Ru^{2+}-labeled CA15-3 secondary antibody (Abs) led to the reduction of R_{ct} (curve f). It seems that the attached Ru^{2+} on the surface interacts electrostatically with [Fe(CN)$_6$]$^{3-/4-}$, leading to the decrease in R_{ct}. The presence of negatively charged CdSe QDs in the structure of the signaling probe, thus establishing an electrostatic repulse force with [Fe(CN)$_6$]$^{3-/4-}$ may be the main reason for increasing in R_{ct} (curve g). The integration of GO in the structure of the signaling probe GO-CdSe-Ru-Abs-(CA15-3)-Ab$_{15}$-MWCNT-dw$_1$SPE resulted in decreasing in R_{ct} (curve h), perhaps due to the higher conductivity of GO that facilitates the rate of electron transfer. Fascinatingly, two semicircles appear in the Nyquist plot wherever GO exists in the structure the signaling probe [24]. The fitting parameters corresponding to

Table 2 Analysis of CA15-3 and CA72-4 in serum sample using the developed immunosensor and ELISA

Sample no.	Subjects	ELISA [CA15-3] (U.ml⁻¹)	Added [CA15-3] (U.ml⁻¹)	Found [CA15-3] (U.ml⁻¹)	CA15-3 R (%)	ELISA [CA72-4] (U.ml⁻¹)	Added [CA72-4] (U.ml⁻¹)	Found [CA72-4] (U.ml⁻¹)	CA72-4 R (%)
(1)	Healthy	6.7 ± 0.6	0	6.6 ± 0.2	99.3	4.6 ± 0.5	0	4.8 ± 0.6	103
			5	11.9 ± 0.4	101		5	9.5 ± 0.3	98.4
			10	16.9 ± 0.5	101		10	14.8 ± 0.5	102
(2)	Healthy	10.4 ± 0.7	0	10.3 ± 0.3	99.2	3.0 ± 0.3	0	3.0 ± 0.3	98.7
			50	60.0 ± 0.3	99.3		50	53.9 ± 0.6	102
			100	111 ± 1	101		100	104 ± 1	101
(3)	Patient	153 ± 1	0	157 ± 2	103	4.9 ± 0.2	0	4.8 ± 0.4	98.0
(4)	Patient	207 ± 2	0	224 ± 1	108	3.4 ± 0.5	0	3.5 ± 0.3	103
(5)	Patient	12.4 ± 0.5	0	12.2 ± 0.3	98.4	38.1 ± 0.4	0	37.6 ± 0.5	98.5
(6)	Patient	34.1 ± 0.6	0	32.9 ± 0.2	96.5	71.6 ± 0.5	0	74.4 ± 0.6	104

various equivalent circuits of the bare and modified electrodes are shown in Table S1 (Supplementary information).

DLS analysis

Figure 3 shows the result of the study on the size distribution of nanoparticles. The mean diameter of CdSe QDs (panel A) and CdSe-Ru-Abs (panel B) were found to be 3.0 and 4.3 nm, respectively. The DLS results also confirmed the broader size distribution of CdSe-Ru-Abs in contrast to CdSe QDs. Moreover, CdSe-Ru-Abs modification with GO (panel C) resulted in slight increase in the mean diameters and appearance of size distributions with the mean center of 105 and 674 nm, relating to the length and diameters of GO-CdSe-Ru-Abs (signaling probe), respectively.

SEM analyses

SEM analysis was used for the characterization of dw_1SPE, $MWCNT-dw_1SPE$, and $CdSe-Ru-Abs-(CA15-3)-Ab_{15}-MWCNT-dw_1SPE$. The SEM image, shown in Fig. 3 (panel D), clearly depicts the smooth surface of the bare dw_1SPE, while in $Ab_{15}-MWCNT-dw_1SPE$, MWCNT has been distributed consistently on the surface of dw_1SPE (Fig. 3, panel E). Also, the SEM image of $GO-CdSe-Ru-Abs-(CA15-3)-Ab_{15}-MWCNT-dw_1SPE$, represented in Fig. 3, panel F, approves a scaly, dense, and porous surface, relating to the settlement of the GO-CdSe QD–based signaling probe on the capture probe.

Optimization of parameters

The optimization of parameters for the effect of MWCNT content on the intensity of ECL signals, amount of antibody conjugation to MWCNT-dwSPE, optimum time for the interaction of analytes with capture probes, and incubation time for GO-CdSe-Ru-Abs are represented in the Supplementary information (S4).

Analytical performance of immunosensor

Calibration curve

As shown in Fig. 4, with the increase in the concentration of CA15-3 and CA72-4, the ECL signal increased and varied linearly with the logarithm of target CA15-3 and CA72-4 concentrations over the range of 10^{-5}–500 U.ml⁻¹ and 10^{-4}–150 U.ml⁻¹ with the limit of detection (LOD) of 9.2 and 89 μU.ml⁻¹, respectively. The calculation of LOD was based on the signal-to-noise ratio (S/N) [25]. LOD was defined as the concentration giving an instrumental signal three times the noise value (S/N = 3). We measured the noise value by using a software and multiplied by 3 to give S_{LOD}. C_{LOD} was

calculated from the calibration curve equation ($S = 569.56 \log C + 2921.9$ for CA15-3 and $S = 575.95 \log C + 2374.4$ for CA 72-4). The results showed that this immunoassay offers the advantage of a broad linear range of detection. However, ECL-based assays provide high sensitivity and broad dynamic range, mainly due to the nature of signal transformation by which an input electrical signal is converted into the optical readout [26]. This property differentiates ECL technique from most other electrochemical methods [27]. In Table 1, some important characteristics of the previously reported CA15-3/CA72-4 biosensors are represented.

Selectivity and interference studies

To assess the specificity of the developed immunosensor, ECL responses of immunosensor to prostate-specific antigen (PSA), myoglobin (Myo), vascular endothelial growth factor (VEGF), epidermal growth factor receptor (EGFR), cortisol (COR), neuron-specific enolase (NSE), human serum albumin (HSA), and carcinoembryonic antigen (CEA) were recorded and compared with the ECL responses of CA15-3 and CA72-4 antigens. As shown in Fig. 5, panel A, the ECL signals showed that our developed biosensor significantly differentiates between CA15-3 ($p < 0.05$)-CA72-4 ($p < 0.05$) and abovementioned biomarkers. The signals originating from adsorption events have the opportunity of hidden interference especially in the concentrations right near the limit of detection (LOD). This type of error can be considered in the determination of concentrations very closely to the LOD value. Based on our calculation, we did not observe a notable interference in the detections near the LOQ.

Reproducibility, stability, and regeneration of the immunosensor

The ECL signal of the immunosensor remained at an almost constant value during 15 consecutive cyclic potential scannings, as shown in Fig. 5, panel B. Relative standard deviation (RSD) of this reproducibility was found to be about 3.1 and 4.9 for GO-CdSe-Ru-Abs-(CA15-3)-Ab$_{15}$-MWCNT-dw$_1$SPE and GO-CdSe-Ru-Abs-(CA72-4)-Ab$_{72}$-MWCNT-dw$_2$SPE, respectively.

Accuracy and real sample analysis

To assess the analytical efficiency of developed immunosensor, determination of CA15-3 and CA72-4 concentration in serum samples was performed. As can be seen in Table 2, the results obtained from developed immunosensor and ELISA are in good agreement without any significant difference. Furthermore, it should be noted that selectivity and sensitivity of the proposed method were not notably affected by other proteins present in the serum sample. The detailed information of real sample analysis is represented in the Supplementary information (S5).

Conclusion

In summary, an electrochemiluminescent immunoassay was developed for the determination of CA15-3 and CA72-4 oncomarkers. Innovation in the preparation of dual-working SPE benefiting from the technology of copper-based PCB and applying chitosan-grafted GO nanosheets to efficiently settle down secondary antibodies and CdSe QDs as an ECL-enhancing element made possible sensitive and affordable detection of these two biomarkers. The developed immunoassay had broad linear ranges and low LOD. By approching lower LOD (9.2 $\mu U.ml^{-1}$ for CA15-3 and 89 $\mu U.ml^{-1}$ for CA72-4), the sensing platform of this immunoassay can be tested for other tumor markers. As the limitations of this work, we examined this platform only with a PMT detector and performed the sequential detection of CA15-3 and CA72-4 biomarkers. Simultaneous or multiplex determination of biomarkers need designing a novel electrode matched with array detectors.

Declarations

Conflict of Interest The authors declare no competing interests. The study and experimental sections were approved by ethics committee of Ardabil University of Medical Sciences, Ardabil, Iran (Approval No: IR.ARUMS.REC.1398.298). Blood samples were taken from cancer patients who were referred by oncologists to Nomooneh Laboratory (Tabriz, Iran) for CA15-3 and CA72-4 quantification. Human serum samples used in this study do not have any identifying information about all the participants that provided written informed consent.

Conflict of interest The authors declare that they have no competing of interests.

References

1. Meng X, Chen X, Wu W, Zheng W, Deng H, Xu L, Chen W, Li Z, Peng H (2019) Electrochemiluminescent immunoassay for the lung cancer biomarker CYFRA21-1 using MoOx quantum dots.

Microchim Acta 186:855. https://doi.org/10.1007/s00604-019-3917-4

2. Huang Z-J, Han W-D, Wu Y-H, Hu XG, Yuan YN, Chen W, Peng HP, Liu AL, Lin XH (2017) Magnetic electrochemiluminescent immunoassay with quantum dots label for highly efficient detection of the tumor marker α-fetoprotein. J Electroanal Chem 785:8–13. https://doi.org/10.1016/j.jelechem.2016.11.060

3. Qin D, Jiang X, Mo G, Zheng X, Deng B (2020) Electrochemiluminescence immunoassay of human chorionic go-nadotropin using silver carbon quantum dots and functionalized polymer nanospheres. Microchim Acta:187. https://doi.org/10.1007/s00604-020-04450-0

4. Chen M-M, Cheng S-B, Ji K, Gao J, Liu YL, Wen W, Zhang X, Wang S, Huang WH (2019) Construction of a flexible electrochemiluminescence platform for sweat detection. Chem Sci 10:6295–6303. https://doi.org/10.1039/C9SC01937E

5. Gao W, Saqib M, Qi L, Zhang W, Xu G (2017) Recent advances in electrochemiluminescence devices for point-of-care testing. Curr Opin Electrochem 3:4–10. https://doi.org/10.1016/j.coelec.2017.03.003

6. Gross EM, Durant HE, Hipp KN, Lai RY (2017) Electrochemiluminescence detection in paper-based and other in-expensive microfluidic devices. ChemElectroChem 4:1594–1603. https://doi.org/10.1002/celc.201700426

7. Guo Z, Sha Y, Hu Y, Wang S (2016) In-electrode vs. on-electrode: ultrasensitive Faraday cage-type electrochemiluminescence immu-noassay. Chem Commun 52:4621–4624. https://doi.org/10.1039/C6CC00787B

8. Chinnadayyala SR, Park J, Le HTN et al (2019) Recent advances in microfluidic paper-based electrochemiluminescence analytical de-vices for point-of-care testing applications. Biosens Bioelectron 126:68–81. https://doi.org/10.1016/j.bios.2018.10.038

9. Duffy MJ, Evoy D, McDermott EW (2010) CA 15-3: Uses and limitation as a biomarker for breast cancer. Clin Chim Acta 411: 1869–1874. https://doi.org/10.1016/j.cca.2010.08.039

10. Wu T, Wang C-H, Wang W, Liu LL, Yun JP, Zhou ZW (2021) Association of preoperative and postoperative CA72-4 with gastric cancer outcome. J Surg Oncol n/a 123:1699–1707. https://doi.org/10.1002/jso.26446

11. Schutter EMJ, Davelaar EM, van Kamp GJ, Verstraeten RA, Kenemans P, Verheijen RHM (2002) The differential diagnostic potential of a panel of tumor markers (CA 125, CA 15-3, and CA 72-4 antigens) in patients with a pelvic mass. Am J Obstet Gynecol 187:385–392. https://doi.org/10.1067/mob.2002.123768

12. Shao H, Lu J, Zhang Q, Hu Y, Wang S, Guo Z (2018) Ruthenium-based metal organic framework (Ru-MOF)-derived novel Faraday-cage electrochemiluminescence biosensor for ultrasensitive detec-tion of miRNA-141. Sensors Actuators B Chem 268:39–46. https://doi.org/10.1016/j.snb.2018.04.088

13. Guo Z, Sha Y, Hu Y, Yu Z, Tao Y, Wu Y, Zeng M, Wang S, Li X, Zhou J, Su X (2016) Faraday cage-type electrochemiluminescence immunosensor for ultrasensitive detection of Vibrio vulnificus based on multi-functionalized graphene oxide. Anal Bioanal Chem 408:7203–7211. https://doi.org/10.1007/s00216-016-9851-y

14. Zhang Q, Hu D, Zhan T, Hu Y, Guo Z, Wang S (2020) Tailored DNA nano-framework-enabled Medusa electrochemiluminescence immunosensor for quantitative detection of histone acetyltransfer-ase. 316:128165. https://doi.org/10.1016/j.snb.2020.128165

15. Nie Y, Wang P, Liang Z, Ma Q, Su X (2021) Rational fabrication of a smart electrochemiluminescent sensor: synergistic effect of a self-luminous Faraday cage and biomimetic magnetic vesicles. Anal Chem 93:7508–7515. https://doi.org/10.1021/acs.analchem.1c00814

16. Shao H, Lin H, Lu J, Hu Y, Wang S, Huang Y, Guo Z (2018) Potential-resolved Faraday cage-type electrochemiluminescence biosensor for simultaneous determination of miRNAs using functionalized g-C_3N_4 and metal organic framework nanosheets. Biosens Bioelectron 118:247–252. https://doi.org/10.1016/j.bios.2018.07.064

17. Lu J, Wu L, Hu Y, Wang S, Guo Z (2018) Ultrasensitive Faraday cage-type electrochemiluminescence assay for femtomolar miRNA-141 via graphene oxide and hybridization chain reaction-assisted cascade amplification. Biosens Bioelectron 109:13–19. https://doi.org/10.1016/j.bios.2018.02.062

18. Wei W, Lin H, Hao T, Su X, Jiang X, Wang S, Hu Y, Guo Z (2021) Dual-mode ECL/SERS immunoassay for ultrasensitive determina-tion of Vibrio vulnificus based on multifunctional MXene. Sensors Actuators, B Chem:332. https://doi.org/10.1016/j.snb.2021.129525

19. Kannan P, Chen J, Su F, Guo Z, Huang Y (2019) Faraday-cage-type electrochemiluminescence immunoassay: a rise of advanced biosensing strategy. Anal Chem 91:14792–14802. https://doi.org/10.1021/acs.analchem.9b04503

20. Johari-Ahar M, Rashidi MR, Barar J, Aghaie M, Mohammadnejad D, Ramazani A, Karami P, Coukos G, Omidi Y (2015) An ultra-sensitive impedimetric immunosensor for detection of the serum oncomarker CA-125 in ovarian cancer patients. Nanoscale 7: 3768–3779. https://doi.org/10.1039/c4nr06687a

21. Zhou X, Zhu D, Liao Y, Liu W, Liu H, Ma Z, Xing D (2014) Synthesis, labeling and bioanalytical applications of a tris(2,2′-bipyridyl)ruthenium(II)-based electrochemiluminescence probe. Nat Protoc 9:1146–1159. https://doi.org/10.1038/nprot.2014.060

22. Bao H, Pan Y, Ping Y, Sahoo NG, Wu T, Li L, Li J, Gan LH (2011) Chitosan-functionalized graphene oxide as a nanocarrier for drug and gene delivery. Small 7:1569–1578

23. Lu J, Wu L, Hu Y, Wang S, Guo Z (2017) Faraday cage-type electrochemiluminescence biosensor based on multi-functionalized graphene oxide for ultrasensitive detection of microrna-21. J Electrochem Soc 164:B421–B426. https://doi.org/10.1149/2.0831709je

24. Casero E, Parra-Alfambra AM, Petit-Domínguez MD, Pariente F, Lorenzo E, Alonso C (2012) Differentiation between graphene ox-ide and reduced graphene by electrochemical impedance spectros-copy (EIS). Electrochem commun 20:63–66. https://doi.org/10.1016/j.elecom.2012.04.002

25. Pedersen-Bjergaard S, Gammelgaard B, Halvorsen TG (2019) Introduction to pharmaceutical analytical chemistry. John Wiley & Sons

26. Ma C, Cao Y, Gou X, Zhu J-J (2020) Recent progress in electrochemiluminescence sensing and imaging. Anal Chem 92: 431–454. https://doi.org/10.1021/acs.analchem.9b04947

27. Liu Z, Qi W, Xu G (2015) Recent advances in electrochemiluminescence. Chem Soc Rev 44:3117–3142

28. Jiang X, Wang H, Yuan R, Chai Y (2015) Sensitive electrochemiluminescence detection for CA15-3 based on immobilizing luminol on dendrimer functionalized ZnO nanorods. Biosens Bioelectron 63:33–38. https://doi.org/10.1016/j.bios.2014.07.009

29. Babamiri B, Hallaj R, Salimi A (2018) Ultrasensitive electrochemiluminescence immunoassay for simultaneous deter-mination of CA125 and CA15-3 tumor markers based on PAMAM-sulfanilic acid-Ru (bpy) 32+ and PAMAM-CdTe@CdS nanocomposite. Biosens Bioelectron 99:353–360

30. Ke H, Zhang X, Huang C, Jia N (2018) Electrochemiluminescence evaluation for carbohydrate antigen 15-3 based on the dual-amplification of ferrocene derivative and Pt/BSA core/shell nano-spheres. Biosens Bioelectron 103:62–68

31. Lv X, Pang X, Li Y, Yan T, Cao W, du B, Wei Q (2015) Electrochemiluminescent immune-modified electrodes based on Ag2Se@ CdSe nanoneedles loaded with polypyrrole intercalated graphene for detection of CA72-4. ACS Appl Mater Interfaces 7: 867–872

32. Fan H, Guo Z, Gao L, Zhang Y, Fan D, Ji G, du B, Wei Q (2015) Ultrasensitive electrochemical immunosensor for carbohydrate antigen 72-4 based on dual signal amplification strategy of nanoporous gold and polyaniline–Au asymmetric multicomponent nanoparticles. Biosens Bioelectron 64:51–56

33. Wu D, Guo Z, Liu Y, Guo A, Lou W, Fan D, Wei Q (2015) Sandwich-type electrochemical immunosensor using dumbbell-like nanoparticles for the determination of gastric cancer biomarker CA72-4. Talanta 134:305–309. https://doi.org/10.1016/j.talanta.2014.11.025

Publisher's note Springer Nature remains neutral with regard to jurisdictional claims in published maps and institutional affiliations.